Key Points:

- Key features of tropical cyclone intensity and size can be captured through empirical orthogonal function analysis of observed winds
- The new, observation-derived phase space provides a useful visualization of tropical cyclone structure evolution
- A new structure parameter related to the radial decay of winds is introduced to represent maturity

Correspondence to:
E. G. Casas,
eleanor.casas@nps.edu

An Intensity and Size Phase Space for Tropical Cyclone Structure and Evolution

Eleanor G. Casas[1] , Dandan Tao[1,2], and Michael M. Bell[1]

[1]Colorado State University, Fort Collins, CO, USA, [2]University of Bergen, Bergen, Norway

Abstract Intensity and size are important to characterize a tropical cyclone (TC), but there are a wide variety of ways that both metrics are defined. TC intensity can refer to either a maximum sustained wind speed at some height level or central surface pressure minimum, and TC size may refer to the radius of maximum wind, the radius of gale force wind, or be based on other criteria. While different definitions of TC intensity and size have useful applications, there are varying amounts of redundant information and covariations between some size and intensity variables that make investigating physical relationships more challenging. In this study, we use aircraft observations and Best Track information to calculate an empirical orthogonal function analysis that yields new, orthogonal metrics of TC intensity and size. The new, linearly independent metrics reduce a seven-dimensional space of co-varying parameters into a simplified, two-dimensional phase space in which key TC structural changes can be visualized and historically contextualized. Additionally, our analysis introduces a new parameter that is a simplified measure of the wind decay outside the radius of maximum tangential velocity. We show that this decay parameter is nearly orthogonal to the new intensity and size metrics and is useful for identifying TC maturity. We demonstrate the utility of the new phase space by first comparing the structural evolution of the large Hurricane Rita (2005) and small Hurricane Charley (2004) using observations, as well as comparing two modeling simulations of Hurricane Rita with different initial conditions in the phase space.

Plain Language Summary Intensity and size are important ways to characterize a tropical cyclone (TC), but there are a variety of ways these metrics are defined. While each definition has its uses, traditional metrics have redundant information, which makes investigating physical relationships more challenging. This study proposes new metrics of intensity and size that are both independent and based on observed variability, as well as introduces a new metric that describes TC maturity. Together, these new metrics distill a lot of information into a simplified, easy-to-understand view of TC intensity and structure, which is demonstrated with observations of Hurricanes Rita (2005) and Charley (2004), as well as with numerical simulations of Hurricane Rita.

1. Introduction

While all tropical cyclones (TCs) have differences in structure that ultimately make each one unique, there are common characteristics that allow us to characterize TCs by various intensity and size metrics. TC structure and intensity are also related to each other, which is demonstrated by the ability to estimate TC intensity from observations of TC structure via satellite imagery using techniques such as the Dvorak method (e.g., Dvorak, 1975; Velden et al., 2006). However, while structure and intensity are intimately related in many ways, the relationships can be complex. For example, it has been known for several decades that there is a weak statistical relationship between static TC intensity and size in terms of the radius of maximum wind (RMW) and maximum tangential wind (V_{max}), which is an attribute of TC structure (Chan & Chan, 2012; Chavas & Emanuel, 2010; Merrill, 1984). This weak statistical relationship between TC intensity and size is due in part to the fact that there is still considerable structural variability across TCs with the same intensity (Xu & Wang, 2015). Additionally, the use of different metrics to describe intensity, structure, or size can yield different relationships and complicate our physical understanding (Chavas et al., 2015).

Variability in size and intensity is also important since anecdotal, statistical, and theoretical studies suggest that TC size can influence future changes in TC intensities and intensification rates (e.g., Carrasco et al., 2014; Hendricks et al., 2014; Rogers et al., 2017; Xu & Wang, 2015). For example, recent research has suggested that the initial TC size strongly impacts evolution throughout the rest of the TC life cycle, such that initially larger

idealized TCs (in terms of RMW and outer radii) can achieve higher steady-state intensities when the environment is constrained to yield TCs with the same maximum potential intensities (Tao et al., 2020; Xu & Wang, 2018). Initial structural variability of the vorticity outside the radius of maximum wind was found to be more important for setting TC expansion rates than environmental moisture in both 2D and 3D idealized CM1 simulations (Chan & Chan, 2015; Kilroy & Smith, 2017; Martinez et al., 2020; Xu & Wang, 2010). Tao et al. (2022) also demonstrate that TC structural evolution is also determined by TC size in addition to TC intensity. Finally, numerous studies have demonstrated through the assimilation of TC observations such as dropsonde, flight-level wind and radar data that improved model representation of TC structure and size can improve forecasts of rapid intensification (Feng & Wang, 2019; Nystrom & Zhang, 2019; Tao et al., 2022; Weng & Zhang, 2016; Zawislak et al., 2022; Zhang et al., 2011). In this study, we seek to simplify the characterization of intensity and size through an examination of the observed variability in wind structure obtained from aircraft reconnaissance.

While the term "TC structure" can refer to a broad array of TC attributes, one of the most commonly observed is TC size. However, there are many different ways to measure TC size depending on the phenomenon of interest. For example, studies that focus on inner-core processes may use the radius of maximum wind (RMW) or the absolute angular momentum at the RMW (M_{max}) (e.g., Schubert & Hack, 1983). In contrast, studies that focus on outer-core processes or TC hazards may use the radius of gale-force winds (R_{34}) instead (e.g., Knaff et al., 2016).

RMW is an important metric to measure because changes in RMW typically correspond with changes in TC intensification. For example, many tropical storms start with a large RMW that contracts as the TC intensifies, and this evolution is often likened to the "ice skater" angular momentum analogy (Stern et al., 2015). However, recent research suggests that RMW contraction often ends before TC intensification is finished (Stern et al., 2015). In addition, fluctuations in the magnitude of RMW are associated with eyewall replacement cycles, which also modulate TC intensification as the inner eyewall decays (Sitkowski et al., 2011).

M_{max} contains both intensity and size information, and it is known to be related to a TC's maximum potential intensity (MPI) (Chavas et al., 2015; Emanuel, 2012; Tao et al., 2020). Since lines of constant angular momentum are often assumed to not penetrate the tropopause, they exhibit a strong constraint on MPI. In addition, since absolute angular momentum increases with increasing radius in an inertially stable vortex, it can be used as a radial coordinate known as 'potential radius'. In this case, M_{max} is related to a TC's "dynamic size," and tight radial gradients near M_{max} are stretched to show detail (e.g., Martinez et al., 2019; Schubert & Hack, 1983).

R_{34} is also an important variable because it is used for forecasting potential hazards and damage extents (Knaff et al., 2016). In addition, the magnitude of R_{34} is linked to other changes in structure, such as the likelihood of secondary eyewall formation or other inner-core structures (e.g., Musgrave et al., 2012; Rozoff et al., 2012; Xu & Wang, 2015), and the magnitude of R_{34} is also related to future intensification rates (Xu & Wang, 2015).

Although related, these three different size parameters do not necessarily co-vary together (Carrasco et al., 2014). Therefore, the concept of TC fullness has been proposed, which is defined as TCF $\equiv 1 - $ RMW/R_{34} (Guo & Tan, 2017). Fullness is highly correlated with intensity, and a rapidly increasing fullness is also associated with current rapid intensification.

While fullness can be considered a measure of TC "shape," it does not directly consider intensity in its definition. The rate of decay of wind from the RMW to R_{34} also varies and is often approximated by a modified Rankine decay parameter (Mallen et al., 2005). However, recent research suggests that the rate of decay of wind outside the RMW is quasi-linear with respect to normalized angular momentum (M^*) (Martinez et al., 2017; Tao et al., 2022). Therefore, in this study, we define the slope of the quasi-linear M^* radial profile as ϕ and show that this new parameter is related to TC maturity.

In addition to having multiple different TC size parameters, there are also multiple ways to define TC intensity, such as the maximum sustained wind speed or minimum central pressure. The maximum wind speed (V_{max}) is a primary way of characterizing intensity (e.g., Simpson, 1974), but there are several variations in how it is defined depending on the wind-averaging period and altitude. In this study, we define V_{max} as the azimuthally averaged flight-level tangential velocity, and use "surface intensity" to refer to the Best Track (BT) 1-min sustained surface wind speed as defined by the U.S. National Hurricane Center.

Intensity is also commonly quantified as the minimum central surface pressure (P_{min}) of the TC. Recent research suggests that P_{min} correlates better with TC size and total damage than V_{max} (Klotzbach et al., 2020), and acts as

a relatively good evaluation metric for TC structure (Tao et al., 2022). While most global estimates of P_{min} rely on satellite-based estimates in the absence of in-situ observations (Knapp et al., 2013), it can be measured more accurately and easily than V_{max} or surface intensity, because it is a single point that has a lower sampling error, and it is not dependent on azimuthal averages or extrapolations to the surface wind speed. However, P_{min} also contains information on TC size, such that larger TCs have a lower P_{min} than smaller TCs with an equivalent V_{max} (Klotzbach et al., 2020).

Since there are so many intensity and size metrics in use and they all co-vary to varying degrees, a central purpose of the article is to find a relatively independent combination of parameters that more clearly separate intensity and size and better represent the TC life cycle. We seek to find metrics such that size and intensity are more orthogonal in order to better characterize the TC with as few parameters as possible. Finally, we also seek to have the metrics represent the full range of variability of observed structure and apply the new metrics to explain the existing findings.

To satisfy these objectives, we utilize aircraft TC observations and empirical orthogonal functions (EOFs). EOFs have been successfully used for revealing useful information on many atmospheric systems, such as determining the location and strength of the MJO (e.g., Wheeler & Hendon, 2004). By using the EOF on observational data, we are able to reduce the dimensionality of TC intensity and structure into their primary modes of variability, as well as compare past and future data to climatological averages and standard deviations in an orthogonal space. We show further that the size and intensity phase space developed here can be used to validate numerical weather prediction models.

In Section 2, we will define the new wind decay parameter in more detail, describe the datasets used in this study, detail how we perform our EOF, and describe numerical model setups used to show an example of applications of this study. In Section 3, we will describe the results of the EOF as well as demonstrate a useful application. We discuss and summarize the key findings in Section 4.

2. Methods

2.1. A New Wind Decay Parameter

Since the slope of M^* outside the RMW has been shown to be quasi-linear in both composites of aircraft observations and numerical simulations (Martinez et al., 2017; Tao et al., 2022), we can simply use an angle to represent its slope. We consider this slope as TC "maturity," which we define as a measure of how close a TC is to its quasi-steady state. In contrast to other wind decay profiles that are based on potential intensity theory (e.g., Chavas et al., 2015; Emanuel & Rotunno, 2011), inner-core wind profiles reconstructed from ϕ and M^* are simpler and do not require environmental parameters such as C_K and C_D.

The new maturity parameter, ϕ, is formally defined as the angle with respect to the y-axis in normalized r^* and M^* space, such that

$$\tan \phi_r \equiv \frac{R^*_{outer} - 1}{M^*_{outer} - 1}, \tag{1}$$

where r^* is the radius normalized by the radius of maximum azimuthally averaged flight-level tangential wind (RMW); M^*_{outer} is the absolute angular momentum normalized by its value at the RMW; R^*_{outer} is a chosen outer radius, and M^*_{outer} is the absolute angular momentum at that chosen radius outside of the RMW and normalized by the magnitude of the absolute angular momentum at the RMW. If one assumes that the outer radius is R_{34}, then ϕ becomes

$$\tan \phi_{R_{34}} = \frac{(1 - \text{Fullness})^{-1} - 1}{M^*_{R34} - 1}, \tag{2}$$

such that fullness is explicitly related to the numerator of ϕ. However, in this study, we define the outer radius as twice the RMW (2RMW), such that

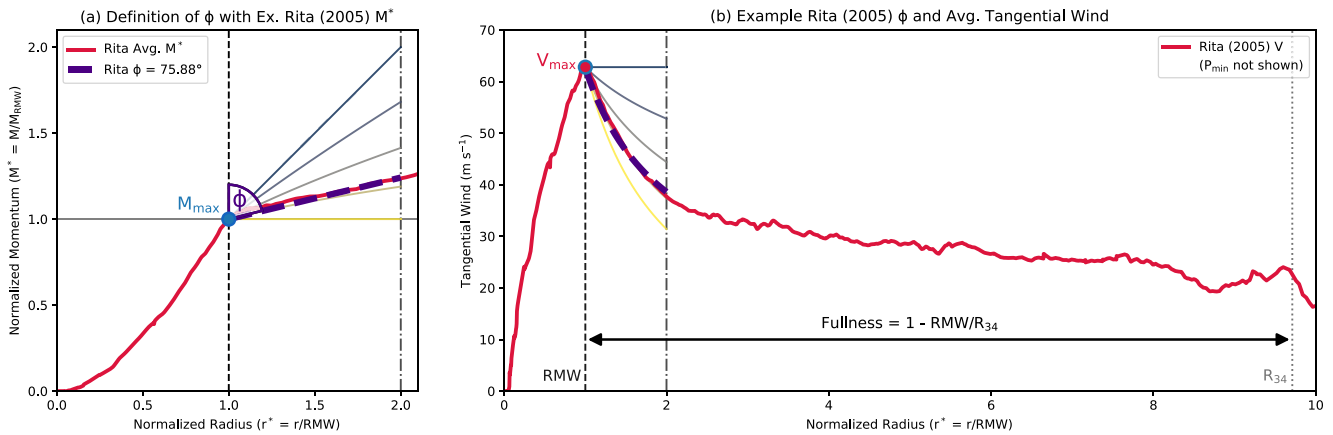$$\tan \phi_{2RMW} \equiv \frac{1}{M^*_{2RMW} - 1}, \tag{3}$$

Figure 1. (a) Definition of ϕ as in Equation 3 (purple angle) with an example M^* profile from Hurricane Rita 2005 at peak intensity (red). The blue to yellow reference lines are equally spaced from 45 to 90 deg. and represent the theoretical upper and lower limit of ϕ. (b) Visual depiction of how the definition of ϕ and additional dataset variables relate to the azimuthally-averaged, flight-level tangential wind profiles, using the same example Rita (2005) flight data at peak intensity as in (a; red line). In both subplots, dataset variables include V_{max} (red point in (b)), M_{max} (blue label in (a) and blue outline in (b)), radius of maximum wind (RMW) (dark gray dash), R_{34} (light gray dotted in (b)), fullness (black arrow in (b)), ϕ (purple angle in (a)), and P_{min} (not shown). Purple dashed line in both subplots shows the extent of the ϕ definition, which extends from the RMW to 2RMW (medium gray dash-dot).

to both sufficiently describe the TC structure and also allow for quantification of this metric with observed flight-level winds. An example of this definition of ϕ_{2RMW} (hereafter ϕ) is in Equation 3 is demonstrated with a profile of both M^* and V in Hurricane Rita (2005) near peak intensity in Figure 1. Note that M_{max} and V_{max} both occur at the RMW, and ϕ is defined with respect to the y-axis such that increasing angles correspond with increasing maturity. Example blue to yellow reference lines that are evenly spaced from 45 to 90 deg. in M^*-space demonstrate how different angles of ϕ translate back to tangential-wind space, such that $\phi = 45$ deg. translates to a flat tangential wind profile, and $\phi = 90$ deg. represents the steepest and most mature TC profile.

Even though M^* is quasi-linear outside of the RMW, the exact value of M^*_{2RMW} can be noisy due to convection and turbulence at flight-level. Thus, we use a best-fit line that is fixed at the point $(1,1)$ to estimate M^*_{2RMW} and therefore ϕ, which is represented by the purple, dashed line in Figure 1. The outer radii of the best-fit line is chosen to be 2RMW in this study because flight-level azimuthal averages often have limited coverage beyond 2RMW due to flight limitations such as distance to land, finite fuel and flight hours, and mission objectives.

If Coriolis is neglected, the ϕ parameter can be related to the modified Rankine alpha parameter through the approximate relationship

$$\tan \phi \approx \frac{r^* - 1}{(r^*)^{1-\alpha} - 1} \tag{4}$$

where r^* is the normalized outer RMW of interest (which we define as 2RMW), and α is the modified Rankine parameter (Figure 1b). Through this relationship, we can see that the minimum angle of ϕ is $45°$ because that would correspond with an α of 0 and that a pure Rankine vortex with an α of 1.0 would correspond with a ϕ of $90°$. Values greater than $90°$ would imply an inertially unstable vortex.

A physical interpretation of ϕ is that an angle of $\phi = 45°$ would be a wind profile that has constant $V = V_{max}$ from 1- 2RMW, implying no wind decay (blue line in Figure 1). This is typically only possible in very weak or immature storms. As a TC matures, the wind decay and alpha typically increase (Mallen et al., 2005), and the angle of ϕ increases. If a TC were to intensify to a pure Rankine vortex with zero vorticity outside the RMW, ϕ would increase to $90°$ (yellow line in Figure 1). However, observed TCs rarely, if ever, reach this condition, and we are interested in discovering what a realistic upper-bound of ϕ is for observed TCs. Overall, we chose to estimate ϕ instead of trying to estimate α because ϕ is more realistic, and simpler to interpret, and the quasi-linear slope of M^* allows for simpler calculations.
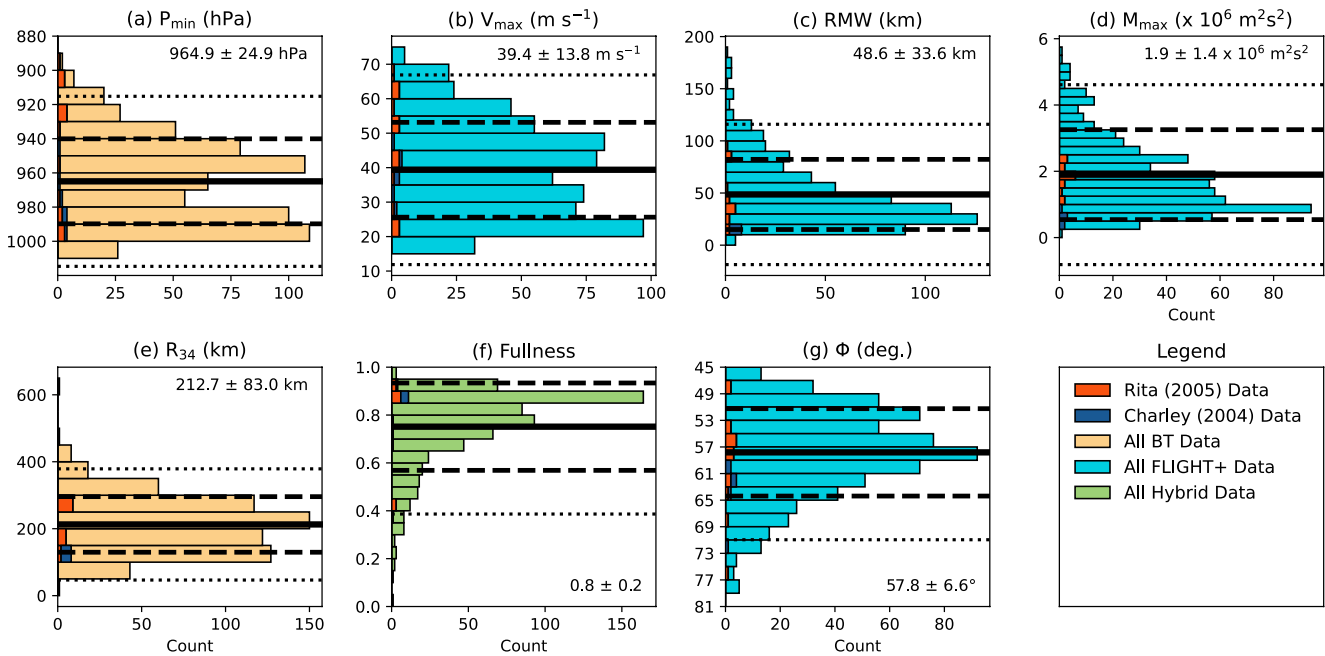
Figure 2. Histograms of the parameters used in this study. Orange and blue represent Hurricanes Rita (2005) and Charley (2004), respectively, and the remaining data is color-coded to denote whether the data source is interpolated from the Best Track (yellow), azimuthally-averaged flight-level data from FLIGHT+ (turquoise), or derived from both datasets (green). Black lines denote each parameter's average (solid), the first standard deviation (dashed), or second standard deviation (dashed) as in Figure 1. The quantitative value of each average and first standard deviation are written on the right-hand side.

2.2. Observational Datasets

We used two observational datasets in this study to derive seven parameters that describe intensity, size, or structure. The first dataset is the Flight Level Dataset (FLIGHT+), version 1.3 (Vigh et al., 2020). We primarily used the binned flight-level tangential wind to compute azimuthal averages from at least three radial legs regardless of quadrant and obtain V_{max}, from which we derived RMW, M_{max}, and ϕ. We also used the RMW from FLIGHT+ to compute fullness (as defined in Section 1), since RMW is not quality controlled in BT estimates prior to 2020 and is not reliably present in BT archives. Though the surface RMW may be slightly smaller than the 700-hPa flight level RMW, they co-vary in a consistent manner (not shown).

We also used two parameters from the International Best Track Archive for Climate Stewardship (IBTrACS; Knapp et al., 2010) dataset to supplement additional parameters of interest, P_{min} and an azimuthal average of available quadrant-dependant R_{34} estimates. In addition to being used as its own parameter, R_{34} was also used to calculate fullness, which means that fullness is the only parameter that was derived from multiple datasets.

The seven parameters used in our EOF analysis (P_{min}, V_{max}, RMW, M_{max}, R_{34}, fullness, and ϕ) are first introduced with respect to an example from Hurricane Rita (2005) in Figure 1. Figure 1a demonstrates the definition of ϕ, and Figure 1b shows the variables relative to the original FLIGHT+ azimuthally-averaged, flight-level tangential wind profile, with the exception of P_{min}, Together, Figures 1a and 1b demonstrate that the seven parameters chosen in this study represent a broad range of attributes that describe both the inner- and outer-core structure of the TC.

The full distributions and data sources of 649 observations of each parameter are shown in Figure 2. Figures 2a and 2b show the azimuthally-averaged flight-level V_{max} and interpolated BT minimum surface pressure P_{min}, with an average P_{min} of 964 hPa and an average V_{max} of 39.4 m s^{-1}. The dataset encompasses a wide range of intensity values about the mean values. Similarly, our three size parameters —RMW, M_{max}, and R_{34} —show that the average of TC observations has values of 48.6 km, 1.9×10^6 m^2 s^2, and 212.7 km, respectively (Figures 2c–2e). Finally, we can see that the mean fullness values are more skewed and have an average of 0.8, and ϕ has a wider range and an average angle of 57.8° (Figures 2f and 2g).

In Section 3.1, we will demonstrate the utility of our EOF analysis by highlighting two examples TCs within our dataset: Hurricane Rita (2005) and Hurricane Charley (2004). Figure 2 shows how our two example TCs compare

to the distributions within the full dataset across their lifetimes. Figures 2a and 2b show that Rita and Charley have observations at nearly the full range of V_{max} and P_{min}. Figures 2c–2e show that Rita and Charley were average sized and small, respectively, compared to other storms. Fullness in Figure 2f shows that Rita and Charley were close to 0.9 through much of their lifecycle, but did have some smaller values at times. Finally, Figure 2g shows that Rita and Charley encompassed a large range of ϕ within the dataset.

2.3. EOF Procedure

The seven variables from the observational datasets were quality-controlled before computing the EOF so we were only using physically-relevant data. The quality control thresholds are.

1. The TCs must have been officially designated as at least a Tropical Storm (TS) for more than 3 hrs such that it has more than one entry in IBTrACs
2. The azimuthal average of V_{max} from binned profiles must contain at least three radial legs in a given flight regardless of quadrant
3. Each flight time must have all seven parameters, including an azimuthal average of available R_{34} estimates
4. ϕ must be less than or equal to 90°.
5. V_{max} must be at least 18 m/s (approximately TS strength)
6. All M^* profiles being averaged must extend out to at least 2RMW

After quality-controlling the data, we had 649 observations from the Atlantic basin available for analysis. We then standardized each parameter with respect to their mean and standard deviation within the dataset before computing the EOF.

Since some of the parameters contain redundant information, we tested many permutations of reduced parameter sets to create the best EOF that explained sufficient variance and had good separation of the different principal components. We also tested an EOF that included Integrated Kinetic Energy as an additional parameter but found that it did not add enough value to warrant inclusion. We found that using all seven of the retained parameters produced the best results since there were sufficient degrees of freedom to determine the primary modes of variance in the observations. Additionally, we also tested the robustness of the EOF structures by repeating the calculations using multiple versions of FLIGHT+, as well as whether restricting the analysis to only intensifying TCs affected interpretation. While there were very minor differences in the resulting EOF structures, the interpretation of the analysis remained the same despite a large difference in sample sizes between the tests.

2.4. Model Setups

In the results section, we also demonstrate a useful application of the EOF by regressing the structure of simulated TCs onto the first two principal components. Here we highlight two variations of Rita (2005) simulations. We chose to highlight Rita as an example because it was well-sampled throughout its lifetime across a wide range of the phase space, which facilitates comparisons between observations and simulations.

The model setup was adapted from Foerster and Bell (2017). We use the Weather Research and Forecasting Model version V3.9.1.1 (WRF; Skamarock et al., 2008) with three nested domains of 18-, 6-, and 2-km horizontal grid spacing and 43 vertical levels. The three domains had 300, 250, and 250 square grid points, respectively, and the two inner domains were vortex-following. The simulations use the following physics parameterizations: Rapid Radiative Transfer Model longwave radiation (Mlawer et al., 1997), Dudhia shortwave radiation (Dudhia, 1989), the Noah land surface model (Ek et al., 2003), the Yonsei University boundary layer scheme (Hong et al., 2006), Thompson aerosol-aware microphysics (Thompson & Eidhammer, 2014), and modified surface fluxes for tropical cyclones (Garratt formulation; Davis & Coauthors, 2008). The outer two domains use the Kain–Fritsch cumulus parameterization (Kain & Fritsch, 1990), and the inner domain is convective permitting. The two WRF simulations were run from 18Z 18 September 2005 to 12Z 23 September 2005 and captured both the period of rapid intensification and the secondary eyewall formation of Hurricane Rita.

We conducted two numerical simulations that were set up identically to each other besides their initial bogus vortex conditions. In particular, we demonstrate the effects of an initially smaller bogus vortex with an initial V_{max} of 17 m s^{-1} and an initial RMW of 150 km, and an initially larger bogus vortex that had an initial V_{max} of 15 m s^{-1} and RMW of 250 km. The model output was smoothed with a Lanczos filter with a window of 100 m with 10 m spacing and a frequency cutoff of 0.001 before regressing onto the EOF to make comparisons easier to interpret.
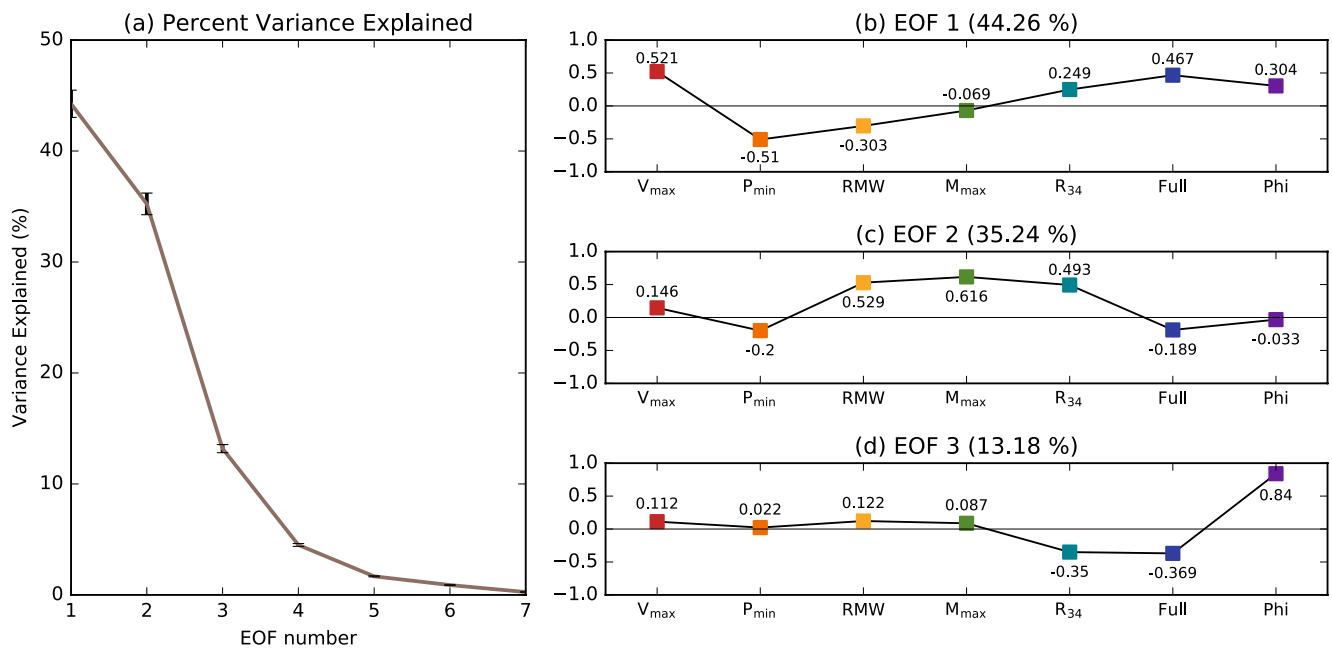
Figure 3. (a) Percent variance explained by each empirical orthogonal functions (EOF) mode, with error bars in black. (b)–(d) The structures of the first three EOF modes. Values indicate the length of the eigenvectors, and rainbow colors are consistent with the arrows in Figure 5.

Model output was then analyzed to be as similar as possible to observations to facilitate comparisons. Variables that were derived from FLIGHT + observations (V_{max}, its RMW, and ϕ) were computed along full azimuthal averages at 700 mb to approximate flight-level heights. R34 was taken from the azimuthally-averaged surface total wind speed. P_{min} was also calculated using the surface level pressure field. Fullness was calculated from the aforementioned RMW and R34 definitions, as in the observational dataset.

3. Results

3.1. EOF Results

Figure 3a shows the percent variance explained by the EOF analysis. Most of the variance is explained by the first two EOFs at nearly 80%. EOF1 primarily represents variability in intensity since the eigenvectors most strongly align with V_{max} and P_{min} (Figure 3b). The variability in wind and pressure is anti-correlated, with positive amplitudes of EOF1 primarily associated with higher V_{max} and lower P_{min}. In contrast, EOF2 primarily represents variability in size since it most strongly depends on RMW, M_{max}, and R_{34} (Figure 3c). EOF1 also has some sensitivity to fullness, RMW, and R_{34}, but there is almost no relationship to M_{max}, while M_{max} is the most dominant parameter in EOF2. Higher fullness, smaller RMW, and larger R_{34} are therefore all correlated with higher EOF1 intensity. A larger RMW, larger M_{max}, and larger R_{34} are all correlated with a larger EOF2 size. The first two EOFs being associated with intensity and then size resulted for every tested permutation of EOF analyses, as well as for stricter quality-control requirements (not shown).

EOF 3 represents approximately 13% of our dataset's variability, and it primarily represents maturity, which is predominately represented by variability in ϕ after accounting for the differences in size and intensity that were already accounted for in EOFs 1–2 (Figure 3d). The fact that ϕ dominates EOF3 indicates that ϕ is a nearly orthogonal parameter to both intensity and size. EOF3 also shows that there is a weak relationship between ϕ and R_{34} and fullness, where TCs with smaller R_{34} are more likely to have higher ϕ angles. EOFs 4–7 represent a combined variability of approximately 7% and are not shown because they are likely associated with noise.

However, while we interpret EOF1 as intensity, EOF2 as size, and EOF3 as "maturity," we note that each EOF contains some information on all three attributes, in accordance with the direction of the eigenvectors. In particular, intensity and maturity seem to have some aspects in common, since a component of ϕ points in the same direction as PC1. Similarly, PC1 also incorporates some size information from RMW and R_{34}, and PC2
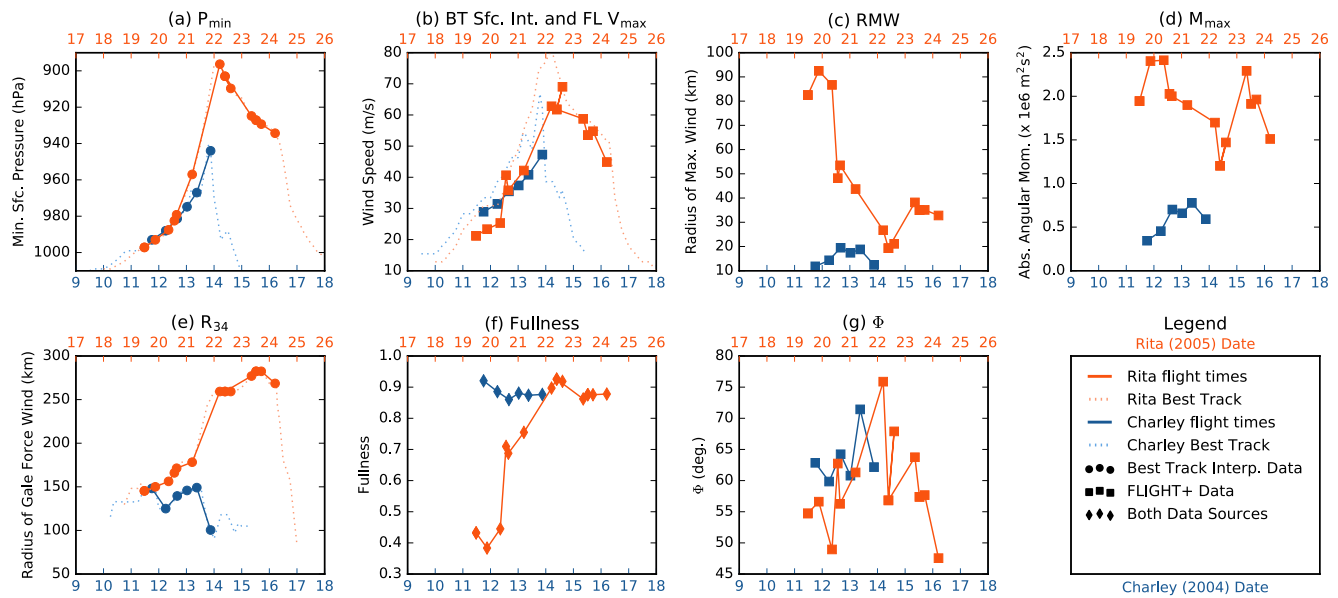
Figure 4. Interpolated Best Track and azimuthally-averaged values for Rita (orange) and Charley (blue) that are included within the empirical orthogonal functions dataset, where the dates for each tropical cyclone are in September 2005 for Rita (top axis) and in August 2004 for Charley (bottom axis). The parameters shown are: (a) All P_{min} (hPa) values (pale solid lines) and interpolated to flight times (circles), (b) All BT Surface Wind Speed estimates (pale solid lines) and FLIGHT + flight-level azimuthal averages (V_{max}; m s^{-1}; squares), (c) RMW (km), (d) M_{max} ($\times 10^6$ m^2 s^2), (e) All R_{34} (km) values (pale solid lines) and interpolated to flight times (circles), (f) Fullness, (g) ϕ (deg). Circles indicate second-order accurate interpolations to the flight time from BT data. Squares indicate azimuthally-averaged values at flight-level from FLIGHT + data. Diamonds indicate that parameters from both datasets were used.

incorporates some intensity information from P_{min}. However, a benefit of this EOF analysis is that we show how each of the seven metrics covaries as TCs evolve.

To more clearly show the relationship between the EOF analysis and physical metrics, Figure 4 shows examples of the lifecycle of Hurricanes Rita (2005) and Charley (2004). These two TCs were chosen to demonstrate how different intensities and sizes are represented in the EOF analysis. Rita (2005) had 16 flights that met the QC criteria, with intensities that ranged from Categories 1–5 on the Saffir–Simpson scale and medium size. In contrast, Charley (2004) was a small, intense TC sampled by six flights.

Figure 4a shows the central minimum surface pressure, which is interpolated from BT data to the average flight time with second-order accuracy finite differencing. Note that the y-axis has been reversed such that lower pressures are at the top for easier comparison. The dates on the two x-axes have been aligned to show that Rita and Charley had a period of similar intensification rates near the beginning of their observations. However, Rita was able to reach much lower P_{min} values at peak intensity than Charley, which may be partly affected by Charley making landfall during the peak of its intensification and partly due to Rita's much larger size.

Figure 4b shows the FLIGHT + azimuthal averages for Rita and Charley in orange and blue, and compares them to the BT estimates of sustained 1-min average surface wind speeds. Comparing the FLIGHT + V_{max} to the surface intensity, there is general agreement with the rate of intensification for both Rita and Charley, but the flight-level tangential velocity averages are consistently lower than the surface wind speed estimates. Comparing the FLIGHT + V_{max} to the interpolated P_{min} evolutions, Rita appears to have a more similar intensity to Charley at the midpoint of the observed periods, rather than the beginning. This could either be due to limitations to azimuthal averages or be related to the very different sizes of Rita and Charley.

Figure 4c shows the RMW of the FLIGHT + azimuthal averages. While some BT estimates were available to compare, they occurred sporadically and are not quality controlled in the official BT process. Thus, they were omitted from the figure. Rita's RMW started out quite large and contracted significantly throughout its intensification period. An eyewall replacement is evident with a larger RMW around 23 September. In contrast, Charley's RMW remained quite small throughout the observed intensification period. Figure 4d shows M_{max}, which is the value used to normalize M profiles to calculate ϕ. M_{max} is obtained from V_{max}, RMW, and the Coriolis parameter, all of which are obtained from the FLIGHT + dataset. The M_{max} magnitude was larger in Rita and
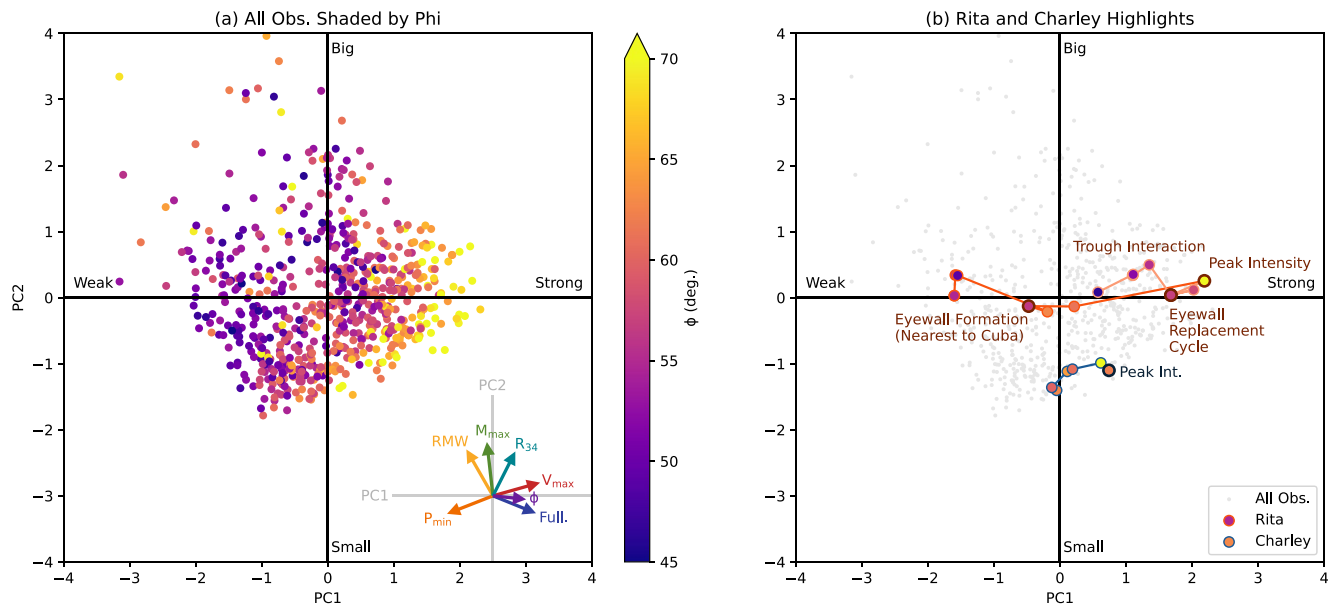
Figure 5. Empirical orthogonal functions dataset transformed into coordinates where PC1 is the x-axis and PC2 is the y-axis. (a) Scatter points of all observations area shaded by ϕ using the same colorbar in Figure 1. Arrows show how the points in Figures 3b and 3c are represented in this phase space, where Figure 3b are the x-components, and Figure 3c is the y-components of each arrow. (b) Gray points represent the same points as in (a), but the Rita and Charley points shown in Figure 4 are highlighted in orange and blue circles, respectively, and filled according to ϕ as in (a). The weakening phase of Rita is outlined with a paler orange to make it easier to see, and the annotated key tropical cyclone lifecycle points are outlined in a bolder and darker color. Additional text labels on the axes are included to help with physical interpretation of both subplots.

decreased as the RMW contracted. Rita's eyewall replacement is also evident in the M_{max} evolution. In contrast, M_{max} is small in Charley and increased over the lifecycle as V_{max} increased while RMW stayed roughly constant.

Figure 4e shows R_{34}, which is also interpolated temporally from BT estimates. Interestingly, Rita's R_{34} consistently increases during intensification while Charley's decreases. Figure 4f shows fullness, which is the only parameter that uses both FLIGHT+ and BT data sources. Charley's fullness remains consistently high during the observing period, while Rita's generally increases throughout its intensification period. Both Rita and Charley have similar fullness around 0.9 at peak observed intensity. Figure 4g shows ϕ, which is calculated from FLIGHT + parameters. While there is some noise apparent in this parameter, there is a trend toward larger angles as both TCs intensify. Rita also shows a decrease in ϕ after peak intensity, unlike fullness.

The seven-parameter timeseries show many aspects of the evolution of Rita and Charley, including both intensity and size changes. Through the EOF analysis, we can reduce the dimensionality to show these changes in the context of other TCs in a simple 2-D phase space corresponding to the magnitude of the first two principal components (PCs). Figure 5 shows the data distribution when we use the first principal component PC1, which represents intensity, as the x-axis and the second principal component PC2, which represents the size, as the y-axis. Since the parameters were normalized prior to computing the EOF, the point (0,0) represents the average intensity and size of a TC in the quality-controlled dataset. The upper-left quadrant represents weak, big TCs, and the lower-right quadrant represents strong small TCs. The upper-right and lower-left quadrants represent strong, big and weak, small TCs, respectively.

In Figure 5a, each dot represents a single observed axisymmetric TC structure. The dots are shaded by the value of ϕ, which can be thought of as a 'vertical' axis corresponding to PC3. The arrows in the lower-left corner are an alternative way of viewing the first two EOFs displayed in Figures 3b and 3c, where the x-component is the magnitude of each parameter in PC1 shown in Figure 3b, and the y-component is the magnitude of each parameter in PC2 shown in Figure 3c. The magnitude of each arrow represents how strongly each parameter projects onto PC1 and PC2, and the direction of each arrow corresponds with the gradient of each parameter from low to high magnitudes. In this format, it's also easier to see that V_{max} aligns most closely with the intensity axis, and M_{max} aligns most closely with the size axis. P_{min} is nearly opposite to V_{max}, but has a marginally larger component in the size direction. RMW also has a slightly larger component in the size axis than R_{34}, but both have a small

component in the intensity axis, which is consistent with the fact that RMW and R_{34} both co-vary with intensification. Fullness and ϕ are primarily associated with intensity, but also increase in the negative PC2 direction (i.e., smaller size). The fact that fullness has a larger PC1-component than both RMW and R_{34} corroborates the findings of Guo and Tan (2017), in which fullness was found to be more correlated with BT intensity than RMW or R_{34}. While ϕ and fullness have very similar angles with respect to PC1 and PC2, ϕ is primarily oriented in the vertical PC3 direction (not shown).

In Figure 5b, the orange- and blue-outlined dots correspond with the observations of Rita and Charley shown in Figure 4, and their shading corresponds to ϕ. First, Rita initially started out in the weak, big quadrant for the first four flights, corresponding to low V_{max} and P_{min} magnitudes and large RMW magnitude on 19 September and early 20 September (Figures 4a–4c). As Rita intensifies and contracts the structure 'moves' down and toward the right in the phase space. Some apparent weakening between the fifth and sixth flights occurs during eyewall formation around 20 September, which largely result from a sharp decrease in ϕ and may have been associated with land interactions with Cuba. Rapid intensification and Rita's peak intensity follow as the TC moves further right with increasing PC1 values. During this time period (21 - 22 September), Rita has large changes in all parameters (Figure 4). However, RMW decreases and R_{34} increases such that their contributions yield little net change in the PC2 direction. Just after peak intensity on the 22nd, there is some evidence of Rita's eyewall replacement cycle, which is represented first as a very slight decrease in PC2 and a larger decrease in PC1 as the inner eyewall contracts and decays, and then followed by both larger PC1 and PC2 values as the secondary eyewall becomes dominant. Finally, after the eyewall replacement cycle, Rita starts interacting with a synoptic-scale, upper-level trough, which shears Rita and further increases Rita's RMW and R_{34} while weakening the TC (Figures 4c and 4e).

In contrast, Charley's structure has some of the smallest PC2 magnitudes in the dataset. Charley was not sampled as extensively as Rita over its lifecycle, but we can see that Charley's evolution appears to increase in size for the first half of its observations, which is largely due to increases in RMW and M_{max}. Interestingly, while P_{min} and V_{max} appear to be reasonably similar in the first few flights of Charley and Rita (Figures 4a and 4b), it becomes much clearer in the PC1 framework that Charley is much further along in its lifecycle and mature than Rita because ϕ and therefore PC1 is much larger in Charley during the first few flights. We can also see that Charley's peak intensity is weaker than Rita's.

Overall, Figure 5 shows a novel way to visualize TC structure and evolution in a phase space where intensity and size are nearly orthogonal. The general maturation of a TC will tend to move primarily from left to right in this phase space with a corresponding increase in ϕ and fullness. However, individual storms can occupy different parts of the phase space and evolve differently depending on their environmental conditions and internal processes. Structural changes such as contraction, rapid intensification, and eyewall replacement cycles can be visualized simply in this framework. The phase space also allows for easy comparison between different TCs and their variability in terms of two standardized variables rather than seven physical parameters.

3.2. Modeling Application

While the aircraft observations provide some indication of a smooth TC structural evolution, they are ultimately distinct snapshots in time. Therefore, we also show two variations of a Rita simulation, one with a small bogus vortex initialization and one with a large bogus vortex initialization, to both demonstrate a comparison between Rita's simulated structure and well-sampled observations and highlight the utility of orthogonal intensity and size axes. Not only do the simulations provide evidence of a smooth TC structural evolution in the PC1/PC2 phase space over time, but they also provide insight into how this framework can be used to validate model performance and potentially construct more realistic synthetic (e.g., "bogus") vortex structures for numerical simulations.

Figure 6 compares the smoothed output from each of the two examples Rita simulations to Rita's BT observations that are shown in Figure 4, and model output was calculated as described in Section 2.4 to facilitate fair comparisons. Periods of the simulation prior to Rita's observation period are denoted differently to represent V_{max} less than 18 m s^{-1} (dashed) or V_{max} greater than 18 m s^{-1} but prior to Rita's observations (pale, thin). The bold portions between 1100 UTC 19 September 2005 and 0500 UTC 21 September 2005 will be the primary focus of the comparison between simulations and observations (hereafter the comparison period).

In each simulation, the evolutions of P_{min} and V_{max} show very similar behavior to each other (Figures 6a and 6b). Prior to the comparison period, both simulations intensify at nearly identical rates. At the beginning of the comparison period on 19 September 2005, there is also good agreement between both simulations and both
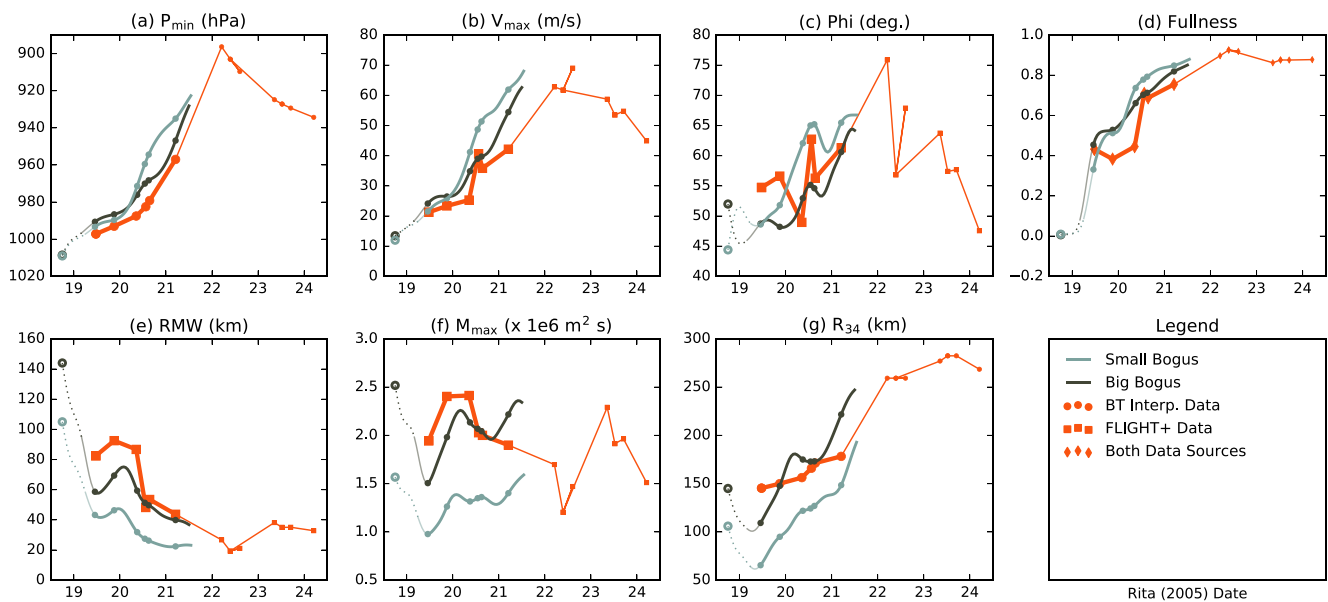
Figure 6. Comparison of the two simulations of Rita to the orange observations shown in Figure 4. Dark blue represents the big-bogus simulation, and light blue represents the small-bogus simulation. The open circle represents the simulation initialization; dotted segment of the simulations represents when $V_{max} < 18$ m s^{-1}, because that portion of the simulation would not meet QC requirements; pale, thin segments of simulations represent that the simulation V_{max} is larger than 18 m s^{-1} but the timing is before Rita's observing period; and bold segments represent the primary comparison time between models and observations. Scatter point symbols for observations are consistent with Figure 4, and equivalent observation times are marked in simulations as well.

the Best-Track P_{min} and FLIGHT + V_{max}. However, on 20 September 2005, the small-bogus simulation begins to intensify more rapidly than both the big-bogus simulation and observations, and the small-bogus simulation remains most intense for the remainder of the simulation time. However, the big-bogus also intensifies but shows signs of an eyewall formation near Cuba. After completing the eyewall formation near Cuba, the big-bogus simulation intensifies at a rate and intensity similar to observations with respect to P_{min}, but V_{max} becomes much more intense than FLIGHT + azimuthal average on 21 September 2005. Overall, the simulation intensities appear to either be reasonably close to observations or an overestimate.

In terms of ϕ and fullness, the big- and small-bogus simulations exhibit similar behavior but with different magnitudes during the main comparison period (Figures 6c and 6d). While both simulations have smaller ϕ and fullness on 19 September 2005 than observations suggest, the small-bogus simulation quickly develops a higher ϕ. In contrast, the big-bogus simulation has a lower ϕ but similar fullness. Both simulations show an interesting ϕ and fullness evolution that is similar to the observations but with different magnitudes. RMW and M_{max} also follow similar evolution at different magnitudes between the big- and small-bogus simulations (Figures 6e and 6f). While both simulations initially contract to an RMW that is too small, the big-bogus simulation magnitudes of RMW and M_{max} end up much closer to FLIGHT + observations than the small-bogus simulation. These results highlight the persistent impact of the initial TC size on future TC evolution (e.g., Martinez et al., 2020; Tao et al., 2020), but a comparison of the time series alone limits the ability to assess how the combined parameters compare to historical vortex structures.

Finally, R_{34} for the big- and small-bogus simulations start out too small at the beginning of the comparison period (Figure 6g). However, the outer-core expansion in the big-bogus simulation becomes similar to observations around 20 September, and then expands too quickly afterward. The small-bogus simulation has too small of an outer wind field for the entire simulation but evolves to just under the observed magnitude around 10Z 21 September 2005. However, the rate of R_{34} expansion in the small-bogus simulation is quite fast compared to observations due to the fast intensification.

Overall, while neither of the simulations was a perfect representation of Rita's evolution, Figure 6 shows that the big-bogus simulation is closer to observations. However, it is hard to separate redundant versus important information in seven panels of comparisons. Figure 7 shows how the two simulations project onto the same coordinates as originally shown in Figure 5. In this format, it becomes much easier to quickly distill the differences between the two simulations. At a glance, we can see that the big-bogus simulation has a larger value of PC2 at all
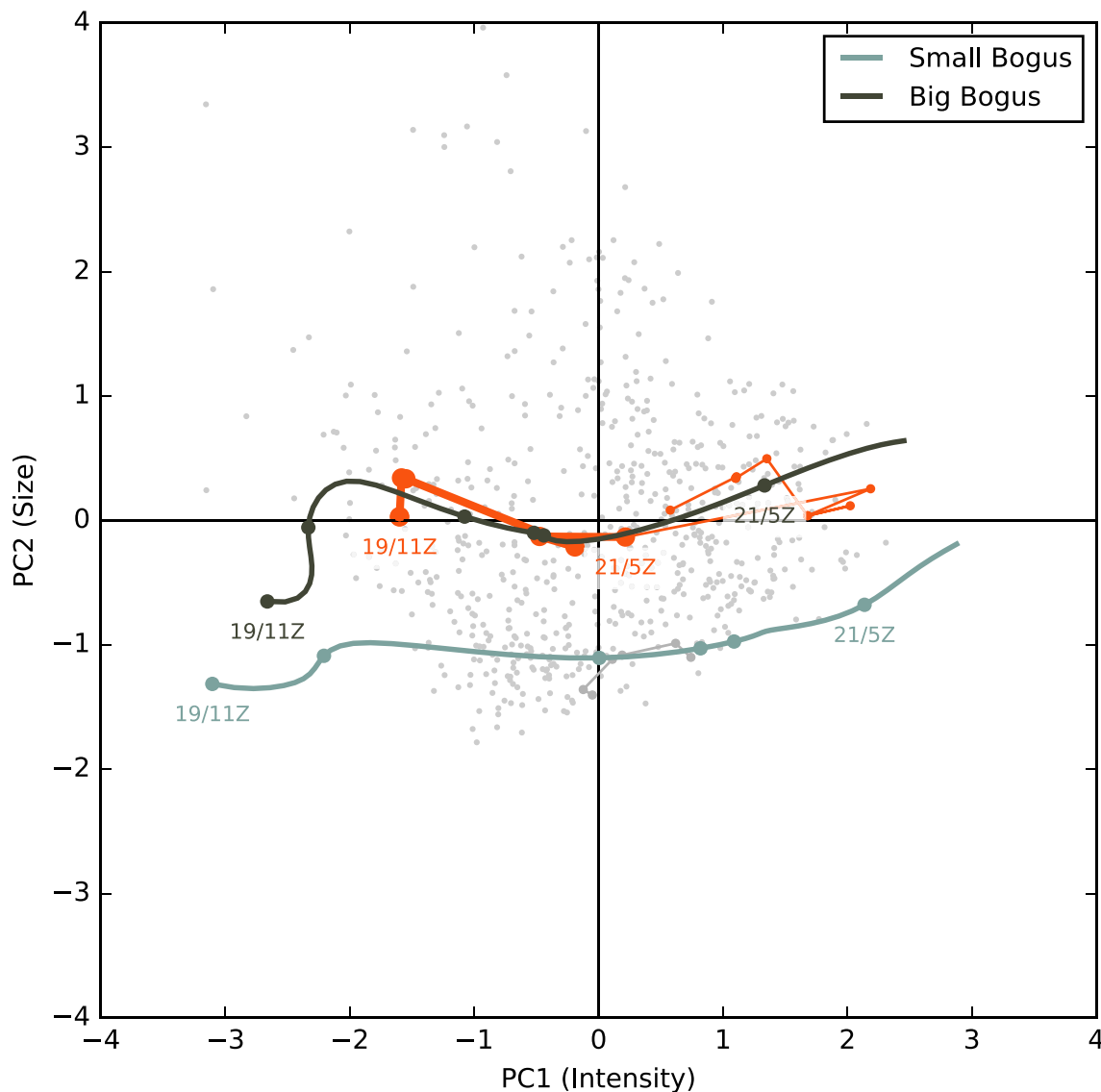
Figure 7. Projections of the big- and small-bogus simulations onto the coordinates shown in Figure 5. The big-bogus simulation is shown in dark blue and the small-bogus simulation is shown in light-blue. Times prior to Rita's observing period have been omitted, but the initial conditions for each simulation are (−5.5, 1.0) for the small-bogus simulation and (−5.0, 2.1) for the big-bogus simulation. Day and hour of first and last observation within the comparison period have been labeled, and points and segments within this time range are bold. Small gray points are identical to Figure 5b.

times than the small-bogus simulation during the comparison period, but the big-bogus simulation is fairly accurate in terms of PC2 size. In addition, we see that the initially big storm remains big with PC2 size. We can also see that the overall structure during the comparison period starts out too weak and ends too intense.

Both simulations show evidence of eyewall formation at the beginning of the comparison period, with a pause in intensification and an increase in size that is similar to observations but in a different part of the phase space. The eyewall formation happens at a much weaker PC1 intensity and smaller PC2 size than Rita's observations would suggest. After that, both simulations slowly contract as they rapidly intensify. Coincidentally, the small-bogus simulation appears to be initialized at an appropriate size for the Charley simulation instead of the Rita simulation, and we can see that the combination of initial conditions led to a small TC compared to observations of Rita. By the end of the comparison period, we can see that the small-bogus simulation has intensified far too quickly with respect to Rita's observations and that PC1 for 05Z 21 September 2005 in the small-bogus simulation is 2 standard deviations more intense than observations. While the initial evolution of the big-bogus simulation is too weak and too small at 11Z 19 September 2005, it is clear that the PC2 size after that adjustment then closely

resembles Rita's observations. However, the simulated storm intensifies too quickly and the PC1 intensity still winds up being 1 standard deviation larger than the observation at 05Z 21 September 2005. To address this remaining error in intensity, additional aspects of the simulation experimental design would have to be addressed, such as synoptic environment or ocean coupling.

Overall, Figure 7 shows the same conclusions as Figure 4 but more concisely. We can see that the big-bogus simulation structure resembles observations the closest, but it is too intense at the end of the simulation. In addition, when combined with the scatter of observed TC variability, we can gain historical context to the curves and quickly identify when there are abnormal intensity-size relationships. While time is implicit in this phase space and must be annotated separately, one can quickly see a holistic TC structural evolution in a single curve. The EOF phase space allows TC researchers and forecasters to quickly identify specific features and examine them in the context of the observed variability.

4. Discussion and Conclusions

In this study, we have used aircraft and BT observations to calculate an EOF analysis and create orthogonal axes for intensity and size. Through the EOF analysis, we have reduced a seven-parameter space into a simplified, orthogonal, 2D phase space, where PC1 is primarily associated with intensity, and PC2 is primarily associated with the size. We also defined a new parameter, ϕ, which is a simple way to characterize vortex radial wind decay. Since our new parameter ϕ primarily corresponds with PC3, we believe that it provides additional information on TC structure and maturity.

However, while our principle components are primarily associated with intensity, size, or maturity, we note that each principle component incorporates some information from the other two attributes. For example, PC1 and "maturity" are related through components of ϕ and fullness, and PC1 also incorporates some size information from RMW and R_{34}. PC2 also retains some intensity information from P_{min} and "maturity" information from ϕ and fullness, as well. However, a benefit of this EOF analysis is that it shows how the seven metrics covary together in such a way that the variability cleanly separates into ways that can be interpreted as intensity and size.

To demonstrate our new intensity-size coordinates, we first compared the well-known storms of Hurricanes Charley (2004) and Rita (2005) within our dataset. When examining individual parameters, we can see noticeable differences in size, but only minimal differences in intensity for the majority of both intensification periods. However, trying to comprehend the various relationships between all seven parameters is challenging. But when plotting onto the EOF phase space, it is more easily apparent that Charley was one of the smallest and more intense TCs in the historical record, while Rita was an averaged size TC that traversed a wide range of PC1 and PC2 values as it intensified, underwent an eyewall replacement, and ultimately weakened.

In addition to comparing observed structure and evolution, we have also demonstrated that simulated structure can be regressed onto these axes for model validation. When comparing two simulations of Rita with initially small and big bogus vortices with BT observations, it is quickly apparent that Rita's initial intensity is similar in both cases but the small-bogus vortex simulation was too small. By increasing the initial RMW, the big-bogus simulation became more in line with the observed structure and evolution. Both simulations intensified too quickly compared to observations, however.

While we have only demonstrated the utility of this framework with deterministic models, this framework could also help distill key structural differences in ensemble runs. The framework could help forecasters more quickly assess deterministic or ensemble simulations, and also allow the ability to quickly put new forecasts and observations into historical context. Researchers can use this framework to diagnose key structural and intensity changes and run more accurate case study simulations by utilizing more realistic initial bogus vortices. Idealized structures can also be compared to real TCs in this framework to determine their realism. For future work, this framework can also be used to assess how variability in the low-dimensional internal structure as presented herein affects contraction, intensification, and other structural evolution in TCs with respect to PC1 and PC2.

Data Availability Statement

Data- FLIGHT+ (Vigh et al., 2020) data of aircraft observations is available at: https://verif.rap.ucar.edu/tcdata/flight/. Data - IBTrACS (Knapp et al., 2010) data of Best Track data is available at: https://www.ncdc.noaa.gov/ibtracs/. Quality controlled and processed data is available upon request.

References

Carrasco, C. A., Landsea, C. W., & Lin, Y.-L. (2014). The influence of tropical cyclone size on its intensification. *Weather and Forecasting*, *29*(3), 582–590. https://doi.org/10.1175/WAF-D-13-00092.1

Chan, K. T. F., & Chan, J. C. L. (2012). Size and strength of tropical cyclones as inferred from quikscat data. *Monthly Weather Review*, *140*(3), 811–824. https://doi.org/10.1175/MWR-D-10-05062.1

Chan, K. T. F., & Chan, J. C. L. (2015). Impacts of vortex intensity and outer winds on tropical cyclone size. *Quarterly Journal of the Royal Meteorological Society*, *141*(687), 525–537. https://doi.org/10.1002/qj.2374

Chavas, D. R., & Emanuel, K. A. (2010). A quikscat climatology of tropical cyclone size. *Geophysical Research Letters*, *37*(18), L18816. https://doi.org/10.1029/2010GL044558

Chavas, D. R., Lin, N., & Emanuel, K. (2015). A model for the complete radial structure of the tropical cyclone wind field. part I: Comparison with observed structure. *Journal of the Atmospheric Sciences*, *72*(9), 3647–3662. https://doi.org/10.1175/JAS-D-15-0014.1

Davis, C., Wang, W., Chen, S. S., Chen, Y., Corbosiero, K., DeMaria, M., et al. (2008). Prediction of landfalling hurricanes with the advanced hurricane wrf model. *Monthly Weather Review*, *136*(6), 1990–2005. https://doi.org/10.1175/2007MWR2085.1

Dudhia, J. (1989). Numerical study of convection observed during winter monsoon experiment using a mesoscale two-dimensional model. *Journal of the Atmospheric Sciences*, *46*(20), 3077–3107. https://doi.org/10.1175/1520-0469(1989)046⟨3077:NSOCOD⟩2.0.CO;2

Dvorak, V. F. (1975). Tropical cyclone intensity analysis and forecasting from satellite imagery. *Monthly Weather Review*, *103*(5), 420–430. https://doi.org/10.1175/1520-0493(1975)103<0420:tciaaf>2.0.co;2

Ek, M. B., Mitchell, K. E., Lin, Y., Rogers, E., Grunmann, P., Koren, V., et al. (2003). Implementation of noah land surface model advances in the national centers for environmental prediction operational mesoscale eta model. *Journal of Geophysical Research*, *108*(D22), 2156–2202. https://doi.org/10.1029/2002JD003296

Emanuel, K. (2012). Self-stratification of tropical cyclone outflow. part ii: Implications for storm intensification. *Journal of the Atmospheric Sciences*, *69*(3), 988–996. https://doi.org/10.1175/JAS-D-11-0177.1

Emanuel, K., & Rotunno, R. (2011). Self-stratification of tropical cyclone outflow. part i: Implications for storm structure. *Journal of the Atmospheric Sciences*, *68*(10), 2236–2249. https://doi.org/10.1175/JAS-D-10-05024.1

Feng, J., & Wang, X. (2019). Impact of assimilating upper-level dropsonde observations collected during the tci field campaign on the prediction of intensity and structure of hurricane patricia (2015). *Monthly Weather Review*, *147*(8), 3069–3089. https://doi.org/10.1175/MWR-D-18-0305.1

Foerster, A. M., & Bell, M. M. (2017). Thermodynamic retrieval in rapidly rotating vortices from multiple-Doppler radar data. *Journal of Atmospheric and Oceanic Technology*, *34*(11), 2353–2374. https://doi.org/10.1175/JTECH-D-17-0073.1

Guo, X., & Tan, Z.-M. (2017). Tropical cyclone fullness: A new concept for interpreting storm intensity. *Geophysical Research Letters*, *44*(9), 4324–4331. https://doi.org/10.1002/2017GL073680

Hendricks, E. A., Schubert, W. H., Chen, Y.-H., Kuo, H.-C., & Peng, M. S. (2014). Hurricane eyewall evolution in a forced shallow-water model. *Journal of the Atmospheric Sciences*, *71*(5), 1623–1643. https://doi.org/10.1175/JAS-D-13-0303.1

Hong, S.-Y., Noh, Y., & Dudhia, J. (2006). A new vertical diffusion package with an explicit treatment of entrainment processes. *Monthly Weather Review*, *134*(9), 2318–2341. https://doi.org/10.1175/MWR3199.1

Kain, J. S., & Fritsch, J. M. (1990). A one-dimensional entraining detraining plume model and its application in convective parameterization. *Journal of the Atmospheric Sciences*, *47*(23), 2784–2802. https://doi.org/10.1175/1520-0469(1990)047⟨2784:AODEPM⟩2.0.CO;2

Kilroy, G., & Smith, R. K. (2017). The effects of initial vortex size on tropical cyclogenesis and intensification. *Quarterly Journal of the Royal Meteorological Society*, *143*(708), 2832–2845. https://doi.org/10.1002/qj.3134

Klotzbach, P. J., Bell, M. M., Bowen, S. G., Gibney, E. J., Knapp, K. R., & Schreck, C. J. (2020). Surface pressure a more skillful predictor of normalized hurricane damage than maximum sustained wind. *Bulletin of the American Meteorological Society*, *101*(6), E830–E846. https://doi.org/10.1175/bams-d-19-0062.1

Knaff, J. A., Slocum, C. J., Musgrave, K. D., Sampson, C. R., & Strahl, B. R. (2016). Using routinely available information to estimate tropical cyclone wind structure. *Monthly Weather Review*, *144*(4), 1233–1247. https://doi.org/10.1175/MWR-D-15-0267.1

Knapp, K. R., Knaff, J. A., Sampson, C. R., Riggio, G. M., & Schnapp, A. D. (2013). A pressure-based analysis of the historical western north pacific tropical cyclone intensity record. Monthly Weather Review, *141*(8), 2611–2631. https://doi.org/10.1175/MWR-D-12-00323.1

Knapp, K. R., Kruk, M. C., Levinson, D. H., Diamond, H. J., & Neumann, C. J. (2010). The international best track archive for climate stewardship (ibtracs): Unifying tropical cyclone best track data. *Bulletin of the American Meteorological Society*, *91*(3), 363–376. [Dataset] https://doi.org/10.1175/2009BAMS2755.1

Mallen, K. J., Montgomery, M. T., & Wang, B. (2005). Reexamining the near-core radial structure of the tropical cyclone primary circulation: Implications for vortex resiliency. *Journal of the Atmospheric Sciences*, *62*(2), 408–425. https://doi.org/10.1175/JAS-3377.1

Martinez, J., Bell, M. M., Rogers, R. F., & Doyle, J. D. (2019). Axisymmetric potential vorticity evolution of hurricane patricia (2015). *Journal of the Atmospheric Sciences*, *76*(7), 2043–2063. https://doi.org/10.1175/JAS-D-18-0373.1

Martinez, J., Bell, M. M., Vigh, J. L., & Rogers, R. F. (2017). Examining tropical cyclone structure and intensification with the flight+ dataset from 1999 to 2012. *Monthly Weather Review*, *145*(11), 4401–4421. https://doi.org/10.1175/MWR-D-17-0011.1

Martinez, J., Nam, C. C., & Bell, M. M. (2020). On the contributions of incipient vortex circulation and environmental moisture to tropical cyclone expansion. *Journal of Geophysical Research: Atmospheres*, *125*(21), e2020JD033324. https://doi.org/10.1029/2020JD033324

Merrill, R. T. (1984). A comparison of large and small tropical cyclones. *Monthly Weather Review*, *112*(7), 1408–1418. https://doi.org/10.1175/1520-0493(1984)112⟨1408:ACOLAS⟩2.0.CO;2

Mlawer, E. J., Taubman, S. J., Brown, P. D., Iacono, M. J., & Clough, S. A. (1997). Radiative transfer for inhomogeneous atmospheres: Rrtm, a validated correlated-k model for the longwave. *Journal of Geophysical Research*, *102*(D14), 16663–16682. https://doi.org/10.1029/97JD00237

Musgrave, K. D., Taft, R. K., Vigh, J. L., McNoldy, B. D., & Schubert, W. H. (2012). Time evolution of the intensity and size of tropical cyclones. *Journal of Advances in Modelling Earth System*, *4*(3), M08001. https://doi.org/10.1029/2011MS000104

Nystrom, R. G., & Zhang, F. (2019). Practical uncertainties in the limited predictability of the record-breaking intensification of hurricane patricia (2015). *Monthly Weather Review*, *147*(10), 3535–3556. https://doi.org/10.1175/MWR-D-18-0450.1

Rogers, R. F., Aberson, S., Bell, M. M., Cecil, D. J., Doyle, J. D., Kimberlain, T. B., et al. (2017). Rewriting the tropical record books: The extraordinary intensification of hurricane patricia (2015). *Bulletin of American Meteorological Society*, *98*(10), 2091–2112. https://doi.org/10.1175/BAMS-D-16-0039.1

Rozoff, C. M., Nolan, D. S., Kossin, J. P., Zhang, F., & Fang, J. (2012). The roles of an expanding wind field and inertial stability in tropical cyclone secondary eyewall formation. *Journal of the Atmospheric Sciences*, *69*(9), 2621–2643. https://doi.org/10.1175/JAS-D-11-0326.1

Schubert, W. H., & Hack, J. J. (1983). Transformed eliassen balanced vortex model. *Journal of the Atmospheric Sciences*, *40*(6), 1571–1583. https://doi.org/10.1175/1520-0469(1983)040⟨1571:TEBVM⟩2.0.CO;2

Simpson, R. H. (1974). The hurricane disaster—Potential scale. *Weatherwise*, *27*, 169–186.

Sitkowski, M., Kossin, J. P., & Rozoff, C. M. (2011). Intensity and structure changes during hurricane eyewall replacement cycles. *Monthly Weather Review*, *139*(12), 3829–3847. https://doi.org/10.1175/MWR-D-11-00034.1

Skamarock, W. C., Joseph, B., Klemp, J. B., Dudhia, J., Gill, D. O., Barker, D., et al. (2008). *A description of the advanced research wrf version 3*. (Tech. Rep.). University Corporation for Atmospheric Research. https://doi.org/10.5065/D68S4MVH

Stern, D. P., Vigh, J. L., Nolan, D. S., & Zhang, F. (2015). Revisiting the relationship between eyewall contraction and intensification. *Journal of the Atmospheric Sciences*, *72*(4), 1283–1306. https://doi.org/10.1175/JAS-D-14-0261.1

Tao, D., Bell, M., Rotunno, R., & van Leeuwen, P. J. (2020). Why do the maximum intensities in modeled tropical cyclones vary under the same environmental conditions? *Geophysical Research Letters*, *47*(3), e2019GL085980. https://doi.org/10.1029/2019GL085980

Tao, D., van Leeuwen, P. J., Bell, M., & Ying, Y. (2022). Dynamics and predictability of tropical cyclone rapid intensification in ensemble simulations of hurricane patricia (2015). *Journal of Geophysical Research: Atmospheres*, *127*(8), e2021JD036079. https://doi.org/10.1029/2021JD036079

Thompson, G., & Eidhammer, T. (2014). A study of aerosol impacts on clouds and precipitation development in a large winter cyclone. *Journal of the Atmospheric Sciences*, *71*(10), 3636–3658. https://doi.org/10.1175/JAS-D-13-0305.1

Velden, C., Harper, B., Wells, F., Beven, J. L., Zehr, R., Olander, T., et al. (2006). The dvorak tropical cyclone intensity estimation technique: A satellite-based method that has endured for over 30 years. *Bulletin of American Meteorological Society*, *87*(9), 1195–1210. https://doi.org/10.1175/BAMS-87-9-1195

Vigh, J. L., Dorst, N. M., Williams, C. L., Stern, D. P., Uhlhorn, E. W., Klotz, B. W., et al. (2020). Flight+: The extended flight level dataset for tropical cyclones (version 1.3) [Dataset]. https://doi.org/10.5065/D6WS8R93

Weng, Y., & Zhang, F. (2016). Advances in convection-permitting tropical cyclone analysis and prediction through enkf assimilation of reconnaissance aircraft observations. *Journal of Meteorological Society Japanese Series II*, *94*(4), 345–358. https://doi.org/10.2151/jmsj.2016-018

Wheeler, M. C., & Hendon, H. H. (2004). An all-season real-time multivariate mjo index: Development of an index for monitoring and prediction. *Monthly Weather Review*, *132*(8), 1917–1932. https://doi.org/10.1175/1520-0493(2004)132⟨1917:AARMMI⟩2.0.CO;2

Xu, J., & Wang, Y. (2010). Sensitivity of tropical cyclone inner-core size and intensity to the radial distribution of surface entropy flux. *Journal of the Atmospheric Sciences*, *67*(6), 1831–1852. https://doi.org/10.1175/2010JAS3387.1

Xu, J., & Wang, Y. (2015). A statistical analysis on the dependence of tropical cyclone intensification rate on the storm intensity and size in the north atlantic. *Weather and Forecasting*, *30*(3), 692–701. https://doi.org/10.1175/WAF-D-14-00141.1

Xu, J., & Wang, Y. (2018). Effect of the initial vortex structure on intensification of a numerically simulated tropical cyclone. *Journal of the Meteorological Society of Japan. Ser. II*, *96*(2), 111–126. https://doi.org/10.2151/jmsj.2018-014

Zawislak, J., Rogers, R. F., Aberson, S. D., Alaka, G. J., Alvey, G. R., Aksoy, A., et al. (2022). Accomplishments of NOAA's airborne hurricane field program and a broader future approach to forecast improvement. *Bulletin of American Meteorological Society*, *103*(2), E311–E338. https://doi.org/10.1175/BAMS-D-20-0174.1

Zhang, F., Weng, Y., Gamache, J. F., & Marks, F. D. (2011). Performance of convection-permitting hurricane initialization and prediction during 2008–2010 with ensemble data assimilation of inner-core airborne Doppler radar observations. *Geophysical Research Letters*, *38*(15), L15810. https://doi.org/10.1029/2011GL048469